Electronic Supplementary Information

Construction of $NiCo_2S_{4-x}P_x$ nanowire arrays for efficient hydrogen evolution reactions in both acidic and alkaline media

Guanglei Liu,[a,b] Yutong Feng,[c] Yifan Yang,[a,b] Yuan Wang,[a,b] Huixiang Liu,[a,b] Can Li,[d] Mingxin Ye[a]* and Jianfeng Shen[a]*

[a] *Institute of Special Materials and Technology, Fudan University, Shanghai 200433, P. R. China.*
[b] *Department of Materials Science, Fudan University, Shanghai 200433, P. R. China.*
[c] *Laboratory of Advanced Materials, Shanghai Key Laboratory of Molecular Catalysis and Innovative Materials, State Key Laboratory of Molecular Engineering of Polymers, College of Chemistry and Materials, Fudan University, Shanghai 200433, P. R. China.*
[d] *College of Optical and Electronic Technology, China Jiliang University, Hangzhou 310018, P. R. China.*
** Corresponding Authors: mxye@fudan.edu.cn; jfshen@fudan.edu.cn*

Experimental Section

Synthesis of NiCo-precursor nanowire arrays on the carbon fiber paper (NiCo-precursor/CFP)

The NiCo-precursor/CFP was synthesized via a hydrothermal reaction. Prior to use, pieces of CFP were treated by acetone, ethanol and deionized water in ultrasonic bath. Then, 1.2 mmol $Ni(NO_3)_2{\cdot}6H_2O$, 2.4 mmol $Co(NO_3)_2{\cdot}6H_2O$, 18 mmol urea were dissolved in 40 mL deionized water inside the Teflon-lined autoclave by ultrasound and stirring methods. A piece of CFP (the upper side of CFP was covered by Teflon tape) was immersed into the above 40 mL mixed reaction solution. The autoclave was sealed by fitted stainless shell and kept at 120 °C for 6 hours in an oven. After the reaction, the product was taken out, washed with deionized water and then dried. Finally, the NiCo-precursor/CFP was obtained.

Synthesis of $NiCo_2S_4$ nanowire arrays on the carbon fiber paper ($NiCo_2S_4$/CFP)

The $NiCo_2S_4$/CFP was synthesized via a hydrothermal reaction with S ion exchange. The prepared NiCo-precursor/CFP was immersed into 30 mL aqueous solution containing 6 mmol $Na_2S{\cdot}9H_2O$ inside the Teflon-lined autoclave. The autoclave was

sealed by fitted stainless shell and kept at 150 °C for 10 hours in an oven. After the reaction, the product was taken out, washed with deionized water and then dried. Finally, the $NiCo_2S_4$/CFP was obtained.

Synthesis of $NiCo_2S_{4-x}P_x$ nanowire arrays on the carbon fiber paper ($NiCo_2S_{4-x}P_x$/CFP)

The $NiCo_2S_{4-x}P_x$/CFP was synthesized via an annealing process with gas-phase phosphorization. Firstly, a porcelain boat containing 110 mg $NaH_2PO_2 \cdot H_2O$ (in the upstream side) and $NiCo_2S_4$/CFP (in the downstream side) was covered with a piece of bare CFP which has a crack in its downstream side (Figure S1), and then the boat was placed in the middle of tube furnace. Secondly, the tube was flushed with Ar gas for several times and then the phosphorization reaction was conducted from room temperature to 350 °C at a heating rate of ~5 °C/min and maintained at 350 °C for 1 hour under the Ar flow. Finally, after naturally cooled down, the $NiCo_2S_{4-x}P_x$/CFP was obtained.

For comparison, different dosages of $NaH_2PO_2 \cdot H_2O$ were carried out in the similar phosphorization strategy of $NiCo_2S_{4-x}P_x$/CFP, and corresponding products were named as $NiCo_2S_{4-x}P_x$/CFP-(l) (50 mg $NaH_2PO_2 \cdot H_2O$) and $NiCo_2S_{4-x}P_x$/CFP-(m) (170 mg $NaH_2PO_2 \cdot H_2O$), respectively.

Characterization

The morphologies and structures of prepared samples were investigated by a scanning electron microscope (SEM, ZEISS Gemini 300) and a transmission electron microscope (TEM, JEOL, JEM-2100F). The crystalline structures of prepared samples were examined by X-ray diffraction (XRD) using a Bruker D8 Advance X-ray diffractometer with Cu Kα radiation. X-ray photoelectron spectroscopy (XPS) was tested by a Thermo Scientific K-Alpha instrument with C 1s peak (284.8 eV) deemed as reference. Raman spectra were measured by a Horiba LabRAM HR Evolution instrument (laser excitation: 532 nm).

Electrochemical measurements

The electrochemical performances were measured in a three-electrode configuration in 0.5 M H_2SO_4 and 1 M KOH aqueous solution at room temperature, by using an

electrochemical workstation (CHI 760E, Shanghai Chenhua Instrument Co., Ltd.). The as-prepared samples ($NiCo_2S_4$/CFP, $NiCo_2S_{4-x}P_x$/CFP-(l), $NiCo_2S_{4-x}P_x$/CFP-(m) and $NiCo_2S_{4-x}P_x$/CFP) were directly applied as working electrodes with a saturated calomel electrode (SCE) and a graphite rod served as the reference electrode and the counter electrode, respectively. Meanwhile, the bare CFP and Pt wire were also applied as working electrodes for comparison. All of the potentials reported in our work were calibrated to the reversible hydrogen electrode (RHE) by adding a value of (0.242 + 0.059 pH) V. Linear sweep voltammetry (LSV) tests were performed at the scan rate of 5 mV s^{-1}, corrected with 85% iR compensation. Electrochemical impedance spectroscopy (EIS) tests were performed at −0.1304 V (vs. RHE) in 0.5 M H_2SO_4 and at −0.13 V (vs. RHE) in 1 M KOH aqueous solution, from 10^5 Hz to 0.1 Hz with an amplitude of 5 mV. Cyclic voltammetry (CV) tests were performed in the range of 0.1996 to 0.2996 V (vs. RHE) at various scan rates (20, 40, 60, 80, 100 and 120 mV s^{-1}) in 0.5 M H_2SO_4 aqueous solution. To investigate the stability of $NiCo_2S_{4-x}P_x$/CFP for hydrogen evolution reaction (HER), the chronopotentiometry tests were implemented at the cathodic current density of 10 mA cm^{-2} for 20 hours in both 0.5 M H_2SO_4 and 1 M KOH aqueous solution, respectively.

Computational Details

All first-principles calculations based on spin-polarized density functional theory (DFT) were conducted in the Vienna Ab-initio Simulation Package (VASP) software. The electron exchange-correlation interactions were described by the Perdew-Burke-Ernzerhof (PBE) functional within the generalized gradient approximation (GGA). The DFT-D3 semiempirical method proposed by Grimme was used to correct the long-range van der Waals interaction. The parameter for dipole correction was also included in our calculations. The GGA + U correction was included for the d-electrons of TM atoms. The convergence criterion for energy and force was set to 1.0×10^{-4} eV and 1.0×10^{-2} eV/Å, respectively. A 5 × 5 × 1 k-point sampling was used for geometric optimization, while a more precise k-point of 6 × 6 × 1 was set to calculate electronic properties. Two surfaces of $NiCo_2S_4$ (311) and $NiCo_2S_{4-x}P_x$ (311) systems were built, where the vacuum space along the z direction is set to be 18 Å, which is enough to avoid interaction

between the two neighboring images. The bottom three atom layers were fixed and the top three atom layers were relaxed to remove the internal stress of systems. Then, the H atom was adsorbed on the Ni, Co, S and P sites, H_2O was adsorbed on the Ni and Co sites, respectively. The complete LST/QST search protocol and the RMS convergence of 0.25 eV/Å are set for transition states.

The absorbed energy (ΔE_{A*}) is calculated by Equation 1:

$$\Delta E_{A*} = E_{A*} - E_{*} - E_{A} \quad (1)$$

where E_{A*} denoted the energy of systems with absorbed A group and E_{*} denoted the energy of systems without absorbed A group (A: H atom or H_2O), and E_A denoted the half energy of H_2 gas or the total energy of H_2O.

The Gibbs free energy change (ΔG_{H*}) of H atom is calculated by Equation 2:

$$\Delta G_{H*} = \Delta E_{H*} + \Delta E_{ZPE} - T\Delta S \quad (2)$$

where the ΔE_{ZPE} and ΔS are the change in zero-point energy and entropy contribution, respectively. T is set to be 300 K and the ($\Delta E_{ZPE} - T\Delta S$) = 0.26 eV for the absorption of H atom.

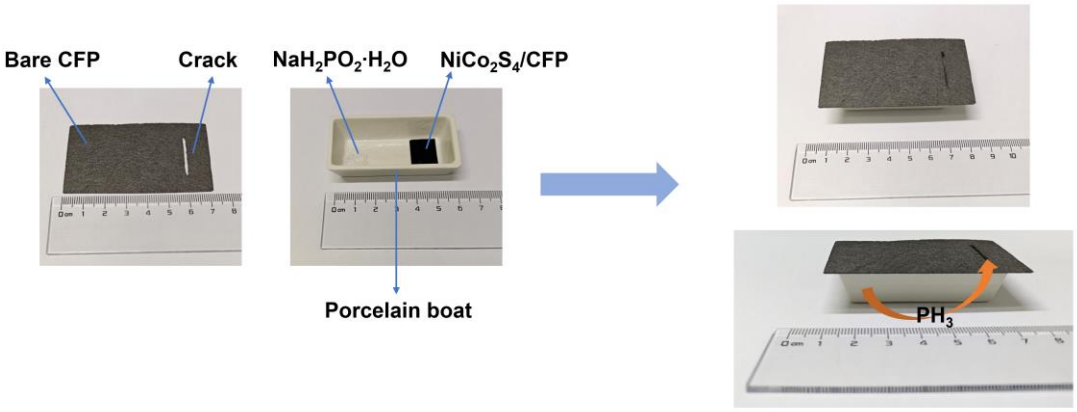

Figure S1. Photographs of the gas-phase phosphorization device: a porcelain boat containing both $NaH_2PO_2 \cdot H_2O$ and $NiCo_2S_4$/CFP, covered with a bare CFP with a crack.

For the gas-phase phosphorization device (Figure S1), a porcelain boat contains upstream $NaH_2PO_2 \cdot H_2O$ and downstream $NiCo_2S_4$/CFP, which is covered with a bare CFP with a crack in its downstream side. During phosphorization process, PH_3 gas derived from $NaH_2PO_2 \cdot H_2O$ can react with metal sulfides to make P doped. This device may not only guarantee sufficient phosphorization for $NiCo_2S_4$/CFP via PH_3 gas flow cross the downstream crack of the bare CFP, but also efficiently weaken the influence from Ar flow speed's unsteadiness.

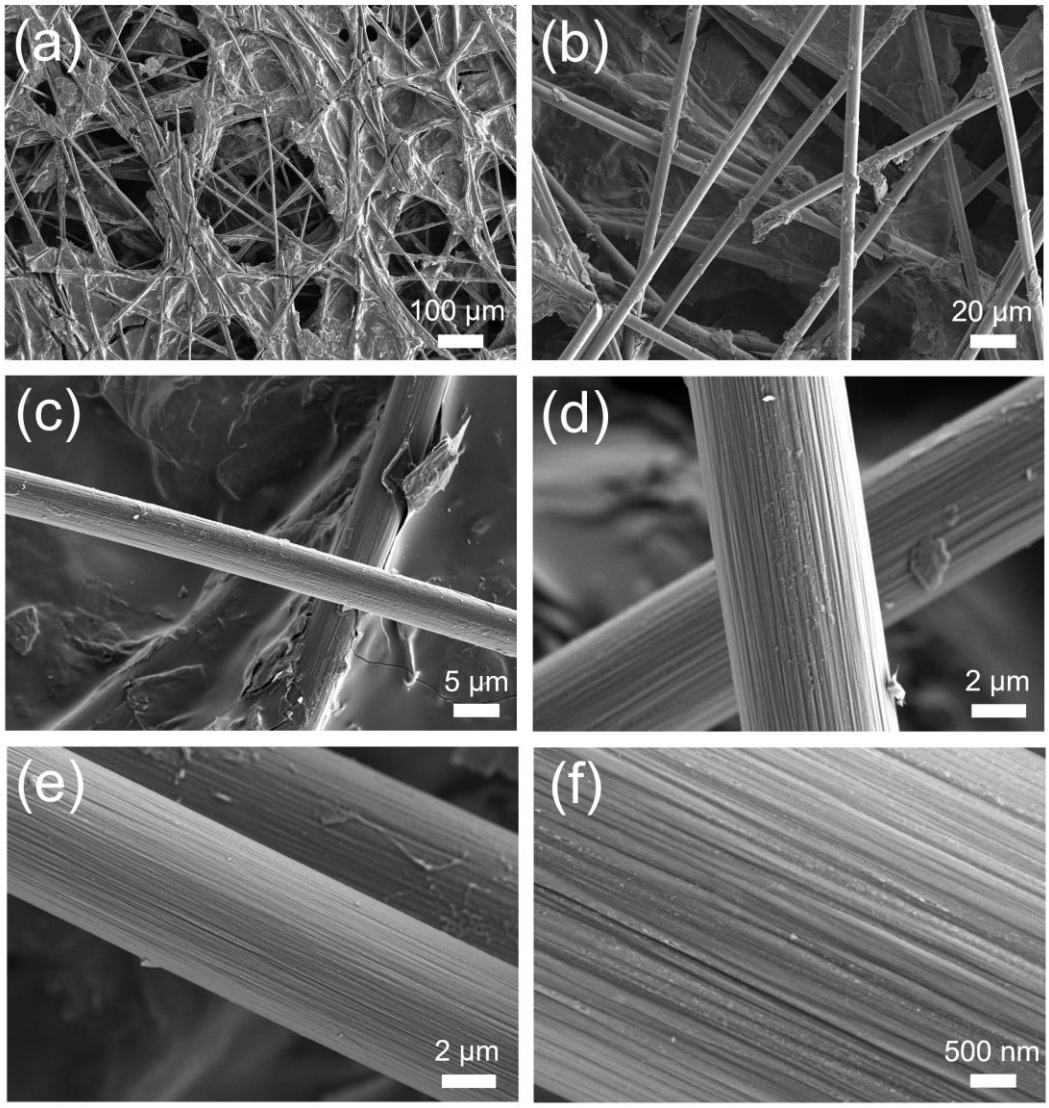

Figure S2. (a−f) SEM images of bare CFP at different magnifications.

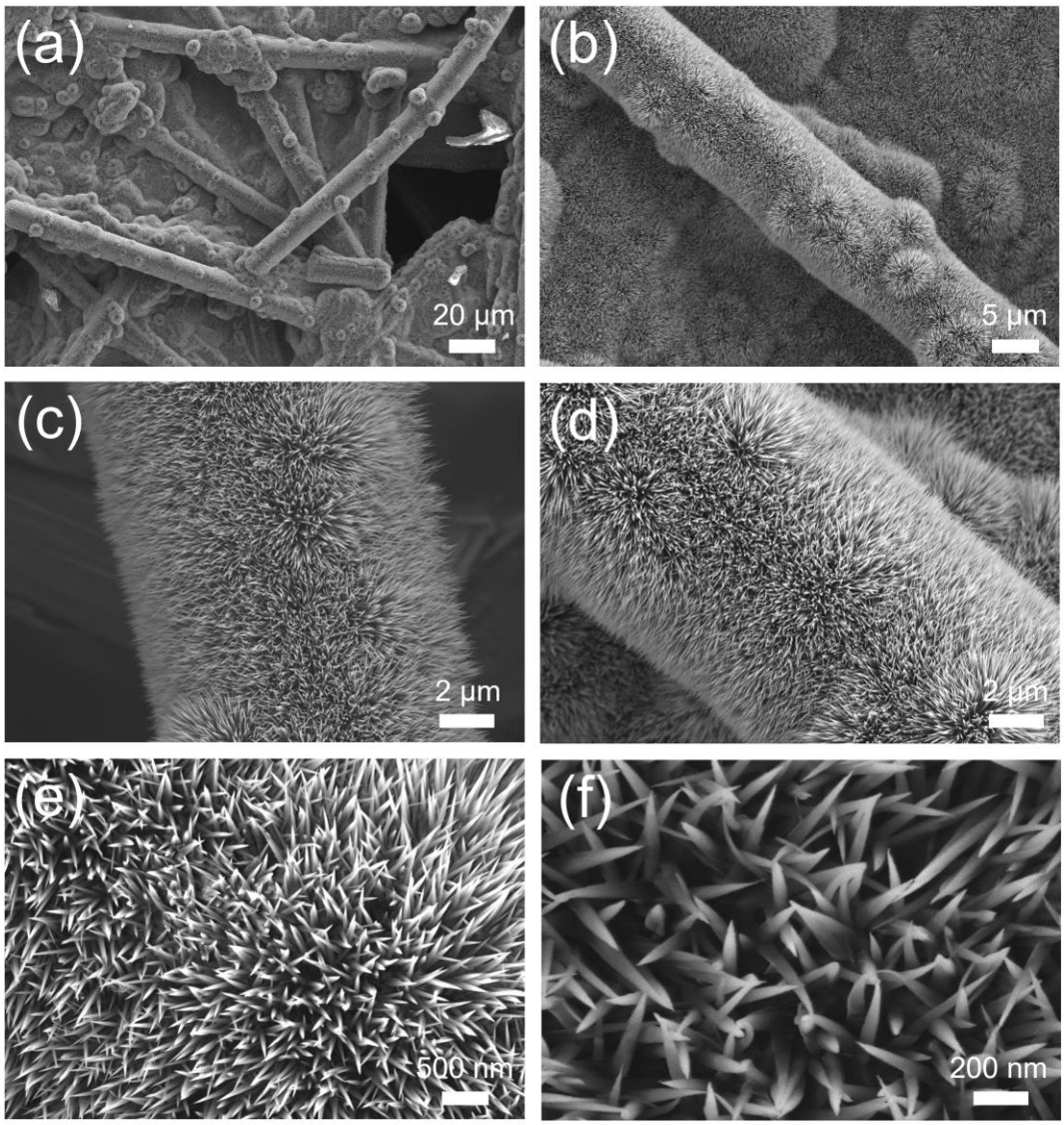

Figure S3. (a−f) SEM images of NiCo-precursor/CFP at different magnifications.

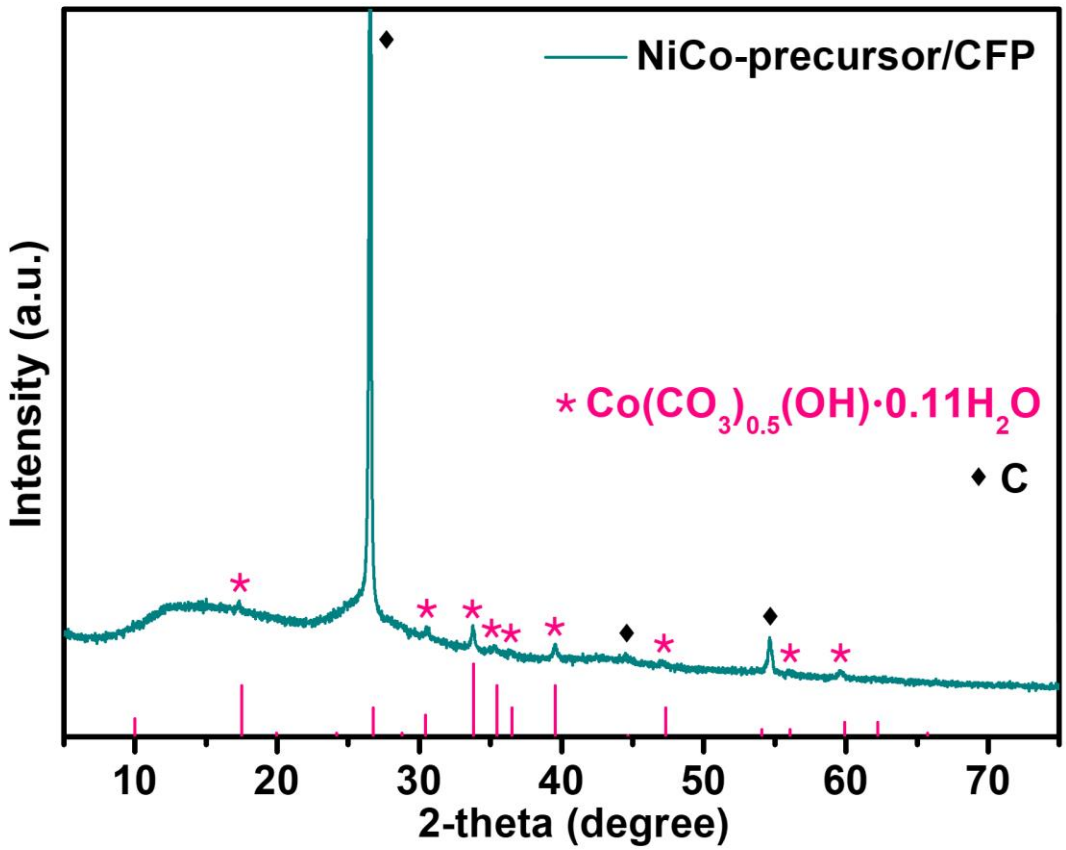

Figure S4. XRD pattern of NiCo-precursor/CFP.

As shown in Figure S4, the XRD pattern of NiCo-precursor/CFP exhibits that these diffraction peaks can be assigned to $Co(CO_3)_{0.5}(OH)\cdot 0.11H_2O$ phase (JCPDS No. 48-0083) except for C phase (JCPDS No. 65-6212) from CFP substrate, which reveals the essential phase of NiCo-precursor 1D nanowire arrays is NiCo-carbonate hydroxide and the partial replacement of Co by Ni does not affect the crystal structure.

Enlightened by relevant works,[1-4] during the hydrothermal process, the urea acts as alkali source and releases OH^- and CO_3^{2-} ions through hydrolysis in solution, and then Ni^{2+} and Co^{2+} ions react with OH^- and CO_3^{2-} ions to form NiCo-carbonate hydroxide grown on CFP. The possible reaction equations are listed as follows:[1, 2]

$$CO(NH_2)_2 + H_2O \rightarrow CO_2 + 2NH_3$$

$$NH_3 + H_2O \rightarrow NH_4^+ + OH^-$$

$$Ni^{2+} + 2Co^{2+} + 6OH^- \rightarrow NiCo_2(OH)_6$$

$$CO_2 + H_2O \rightarrow CO_3^{2-} + 2H^+$$

$$NiCo_2(OH)_6 + 1.5CO_3^{2-} + nH_2O \rightarrow NiCo_2(CO_3)_{1.5}(OH)_3 \cdot nH_2O + 3OH^-$$

As a result, the 1D nanowire arrays of NiCo-carbonate hydroxide are successfully grown on CFP and finally the NiCo-precursor/CFP is obtained.

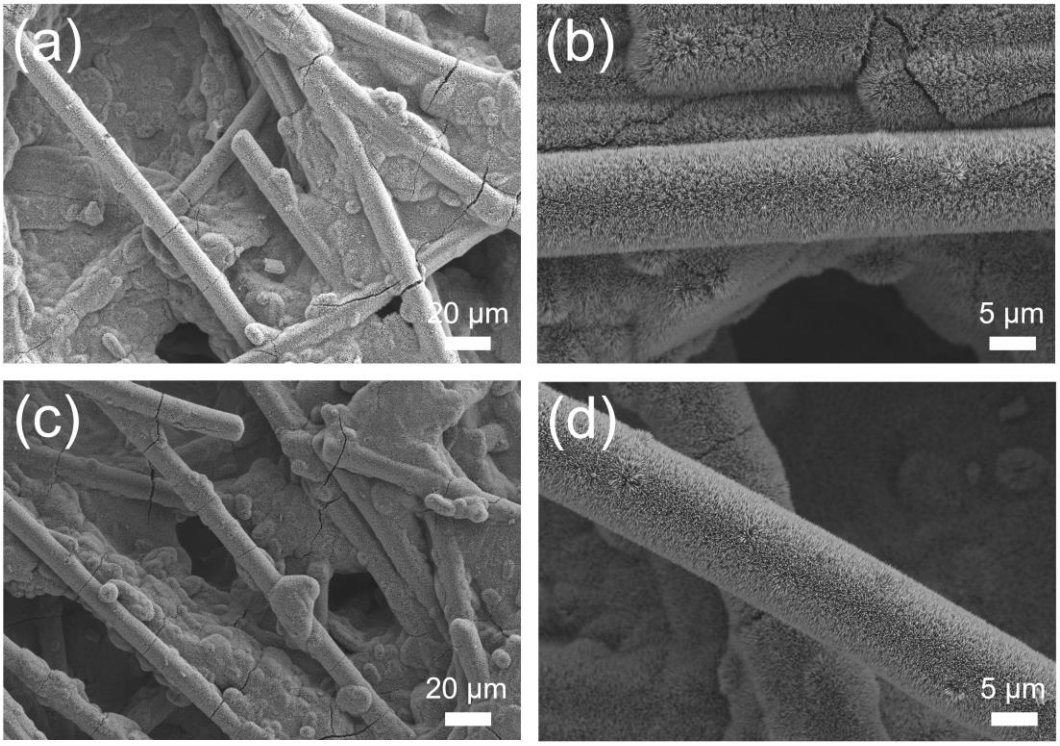

Figure S5. (a, b) Low-magnification SEM images of $NiCo_2S_4$/CFP. (c, d) Low-magnification SEM images of $NiCo_2S_{4-x}P_x$/CFP.

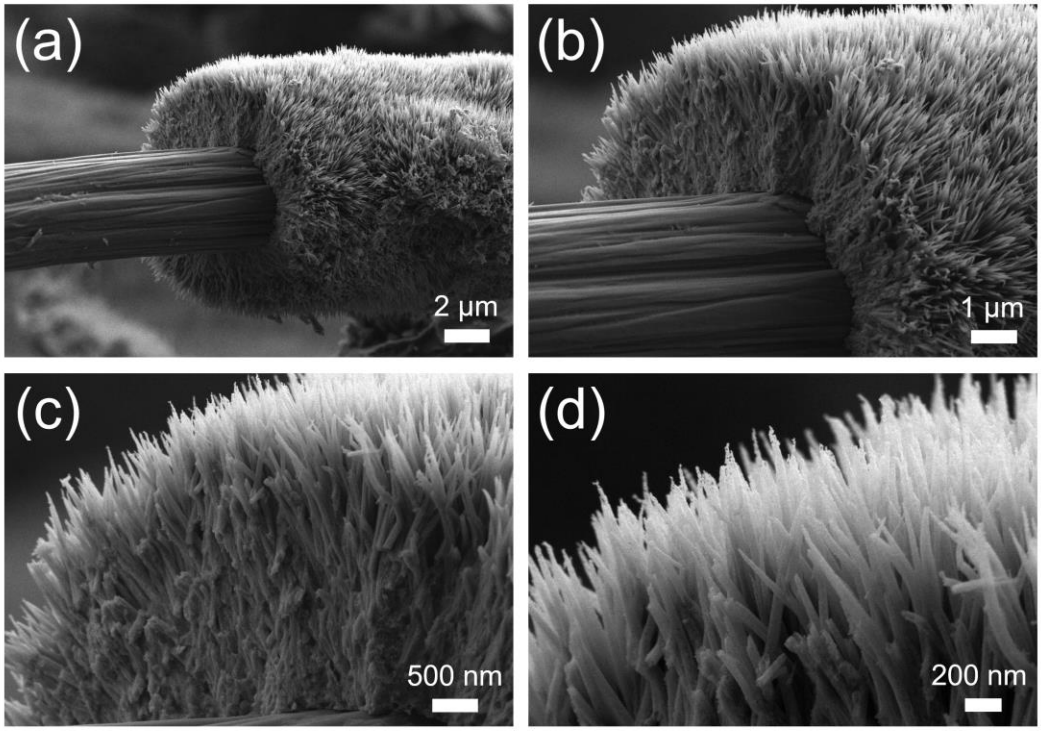

Figure S6. (a−d) Cross-sectional SEM images of $NiCo_2S_4$/CFP.

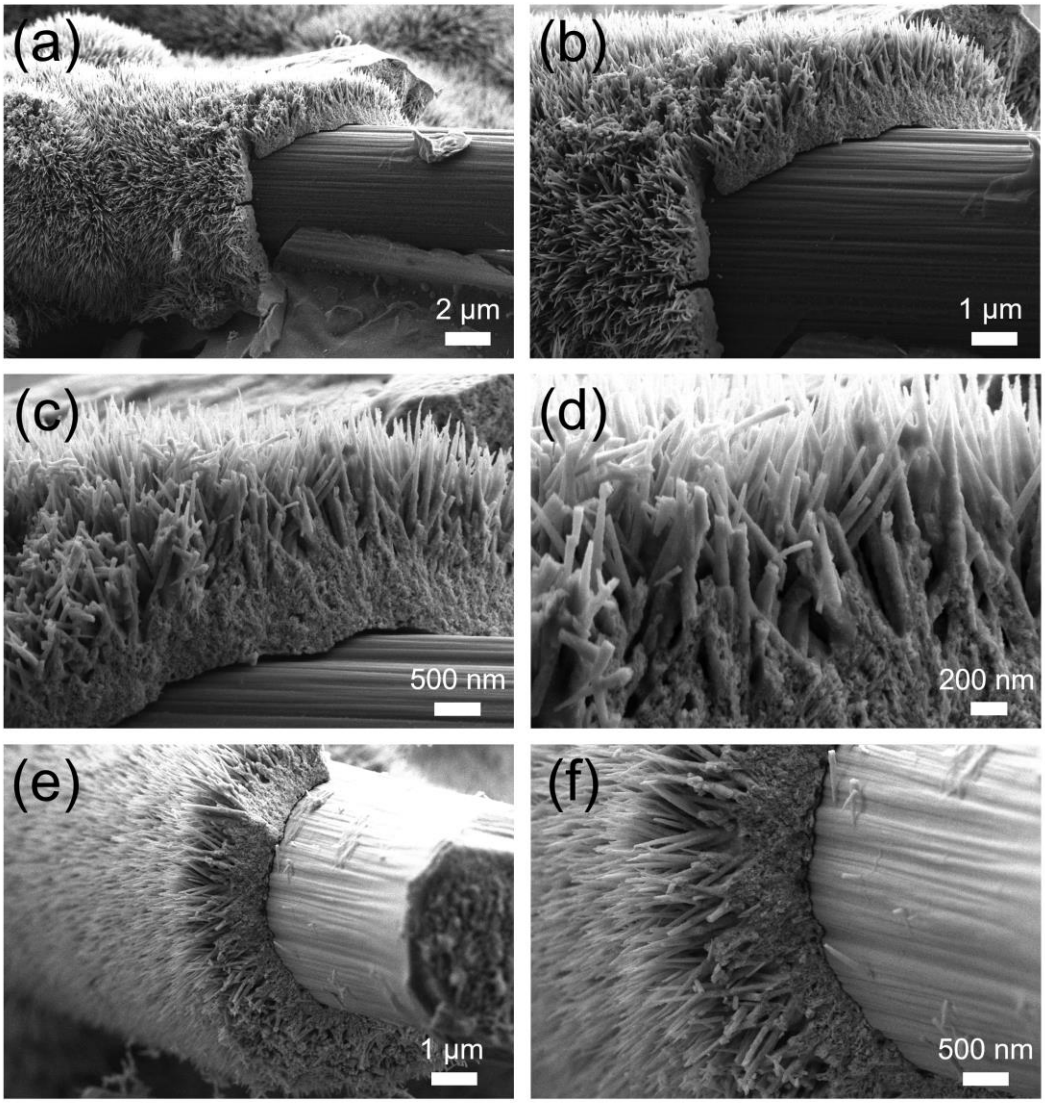

Figure S7. (a−f) Cross-sectional SEM images of $NiCo_2S_{4-x}P_x$/CFP.

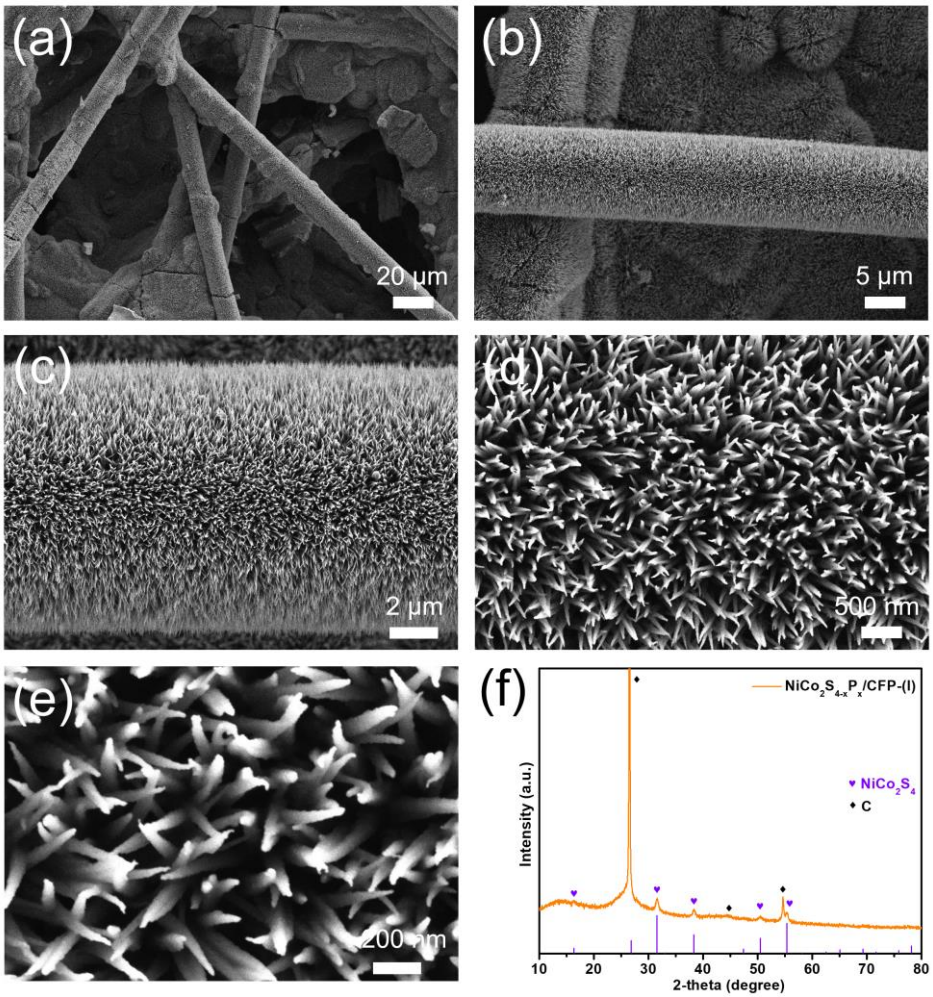

Figure S8. (a−e) SEM images of $NiCo_2S_{4-x}P_x$/CFP-(l) at different magnifications. (f) XRD pattern of $NiCo_2S_{4-x}P_x$/CFP-(l).

The SEM images of $NiCo_2S_{4-x}P_x$/CFP-(l) (Figure S8a−e) show the good uniformity and dispersity of nanowire arrays with coarse surface, similar to $NiCo_2S_4$/CFP and $NiCo_2S_{4-x}P_x$/CFP, which reveals that less dosage of P source does not influence the final morphology and structure in our preparation process. The XRD pattern of $NiCo_2S_{4-x}P_x$/CFP-(l) (Figure S8f) shows that, diffraction peaks match well with cubic crystal phase of $NiCo_2S_4$ (JCPDS No. 20-0782), except for C peaks (JCPDS No. 65-6212) from CFP, which certifies that less dosage of P source in our system can still well maintain the crystal structure of $NiCo_2S_4$ phase.

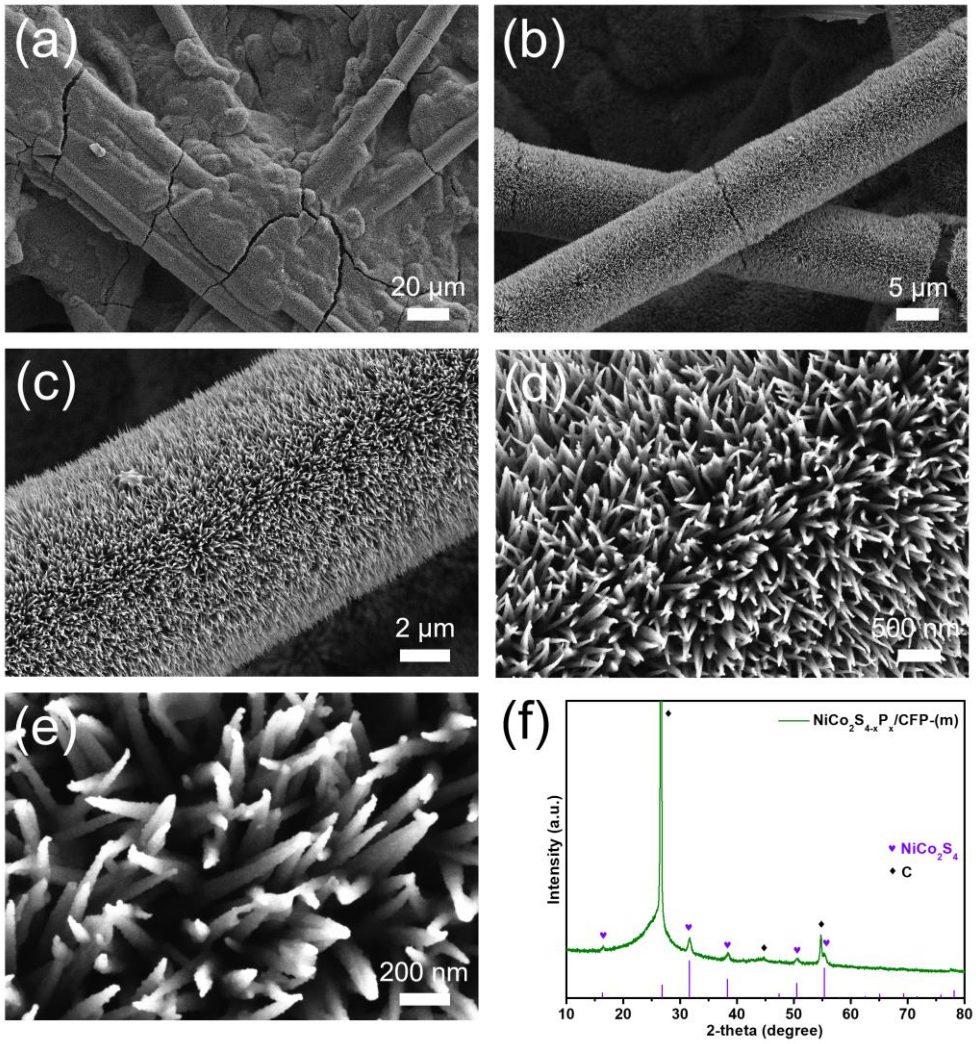

Figure S9. (a−e) SEM images of $NiCo_2S_{4-x}P_x$/CFP-(m) at different magnifications. (f) XRD pattern of $NiCo_2S_{4-x}P_x$/CFP-(m).

The SEM images of $NiCo_2S_{4-x}P_x$/CFP-(m) (Figure S9a−e) show the good uniformity and dispersity of nanowire arrays with coarse surface, similar to $NiCo_2S_4$/CFP and $NiCo_2S_{4-x}P_x$/CFP, which reveals that more dosage of P source does not influence the final morphology and structure in our preparation process. The XRD pattern of $NiCo_2S_{4-x}P_x$/CFP-(m) (Figure S9f) shows that, diffraction peaks match well with cubic crystal phase of $NiCo_2S_4$ (JCPDS No. 20-0782), except for C peaks (JCPDS No. 65-6212) from CFP, which certifies that more dosage of P source in our system can still well maintain the crystal structure of $NiCo_2S_4$ phase.

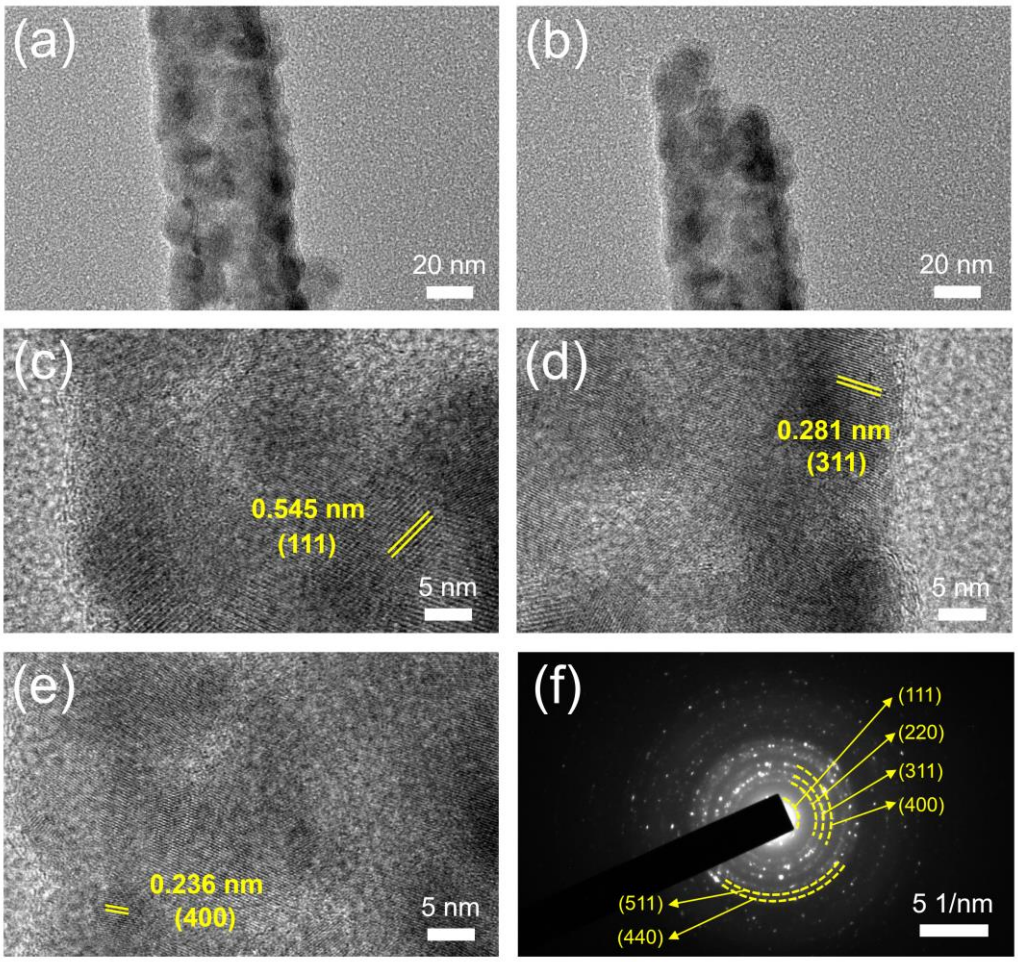

Figure S10. (a−e) Low-magnification TEM images (a, b) and high-magnification TEM images (c−e) of $NiCo_2S_4$. (f) The SAED pattern of $NiCo_2S_4$.

The low-magnification TEM images of $NiCo_2S_4$ nanowires scraped from CFP show clear nanowire profile with coarse surface (Figure S10a, b). The high-magnification TEM images of $NiCo_2S_4$ display well resolved interplanar distances of 0.545 nm (Figure S10c), 0.281 nm (Figure S10d) and 0.236 nm (Figure S10e), assigned to lattice planes of (111), (311) and (400) of the $NiCo_2S_4$ phase, respectively, certifying the successful preparation of $NiCo_2S_4$. The SAED pattern of $NiCo_2S_4$ (Figure S10f) shows a set of diffraction rings, corresponding to (111), (220), (311), (400), (511), (440) lattice planes of $NiCo_2S_4$ phase from the inside out, indicating the polycrystalline nature of $NiCo_2S_4$.

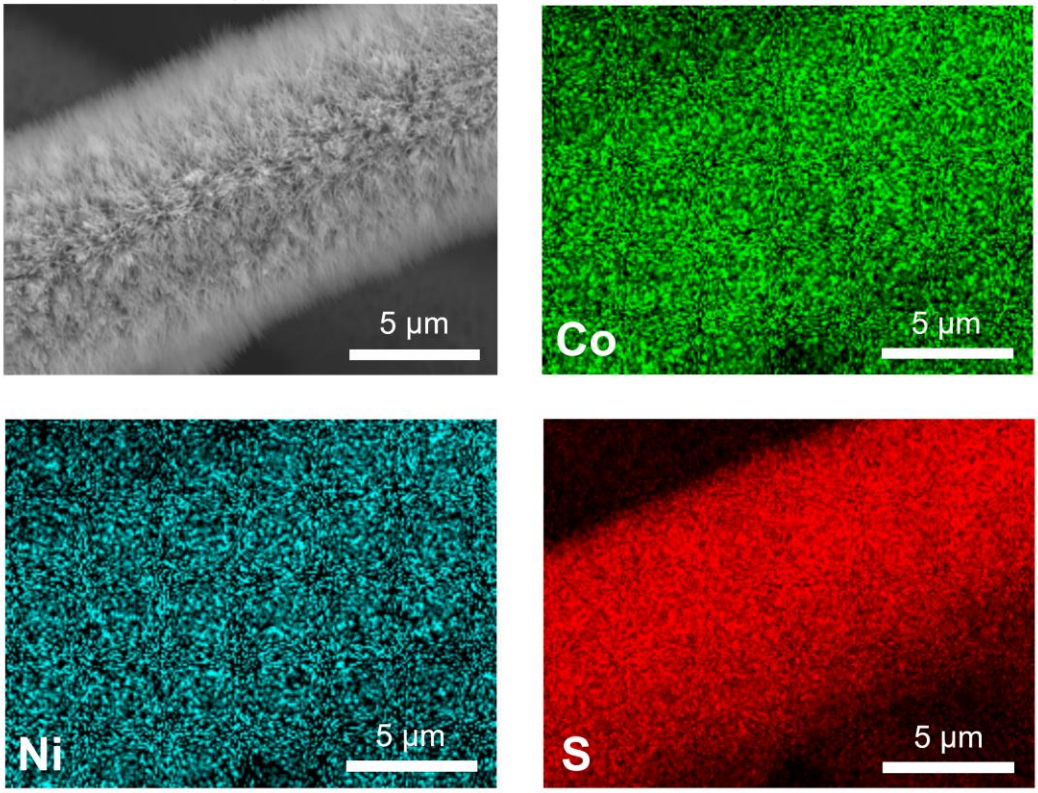

Figure S11. Elemental mapping images of $NiCo_2S_4$/CFP.

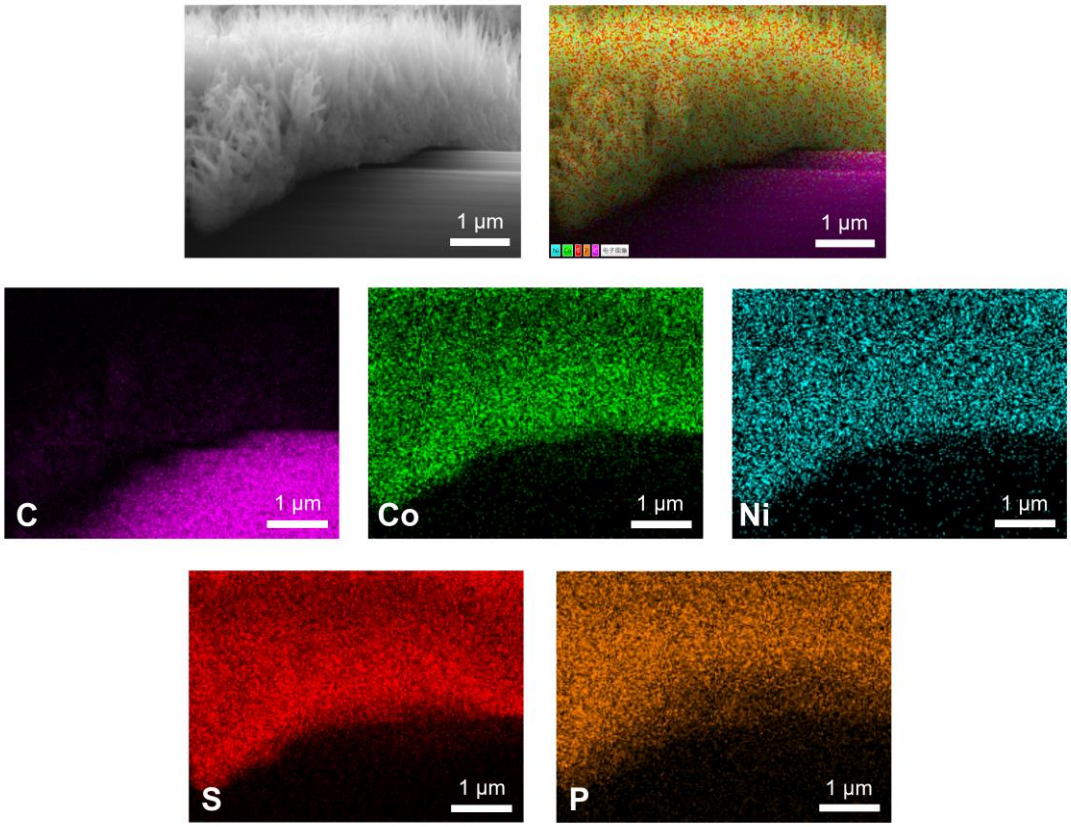

Figure S12. Cross-sectional elemental mapping images of $NiCo_2S_{4-x}P_x$/CFP.

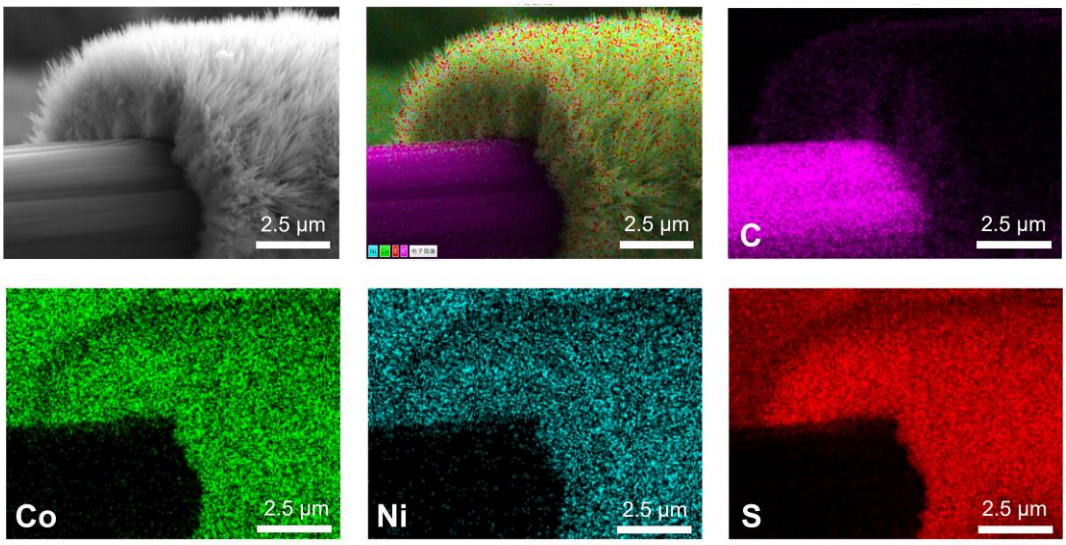

Figure S13. Cross-sectional elemental mapping images of $NiCo_2S_4$/CFP.

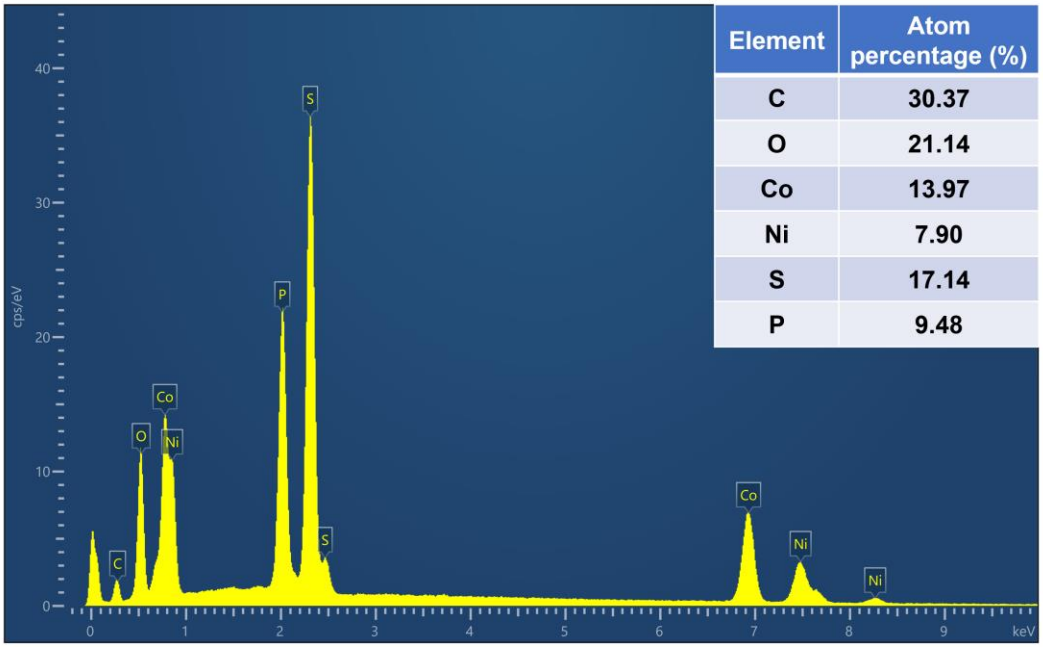

Figure S14. EDS spectrum of $NiCo_2S_{4-x}P_x$/CFP. Inset in EDS spectrum is the relevant atom percentages of different elements.

The EDS spectrum of the $NiCo_2S_{4-x}P_x$/CFP (Figure S14) shows the coexistence of Co, Ni, S, P, C and O elements, where C possibly comes from CFP substrate and O possibly derives from surface oxidation, respectively. Inset in the EDS spectrum (Figure S14) shows the specific atom percentages of Co (13.97%), Ni (7.90%), S (17.14%), P (9.48%) in $NiCo_2S_{4-x}P_x$/CFP, respectively, suggesting the atom ratio of Ni: Co: S: P is approximately 1: 1.77: 2.17: 1.20 and the atom ratio of S: P is approximately 1.81: 1.

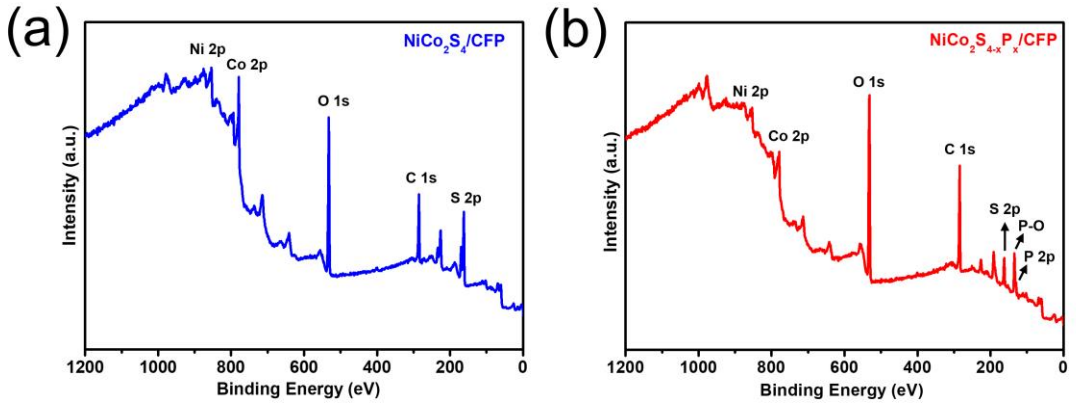

Figure S15. (a, b) XPS survey spectra of $NiCo_2S_4$/CFP (a) and $NiCo_2S_{4-x}P_x$/CFP (b), respectively.

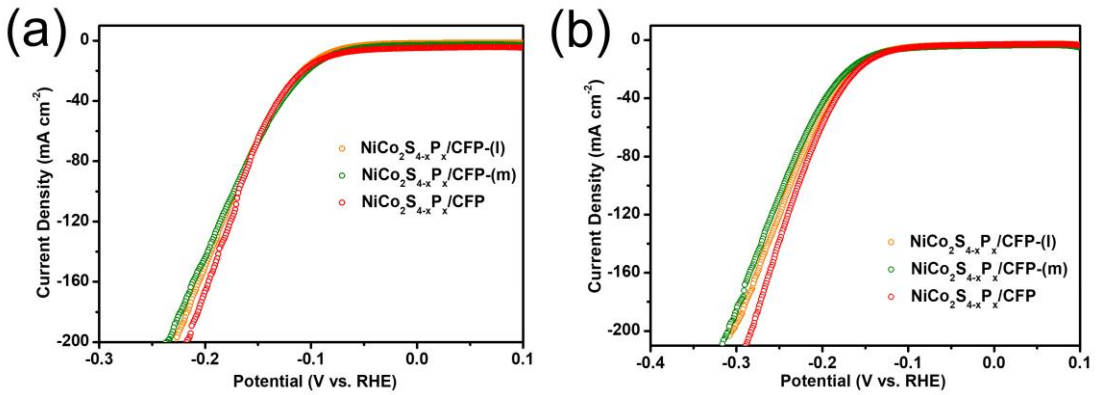

Figure S16. (a) IR-corrected LSV curves of $NiCo_2S_{4-x}P_x$/CFP, $NiCo_2S_{4-x}P_x$/CFP-(l), $NiCo_2S_{4-x}P_x$/CFP-(m) in 0.5 M H_2SO_4. (b) IR-corrected LSV curves of $NiCo_2S_{4-x}P_x$/CFP, $NiCo_2S_{4-x}P_x$/CFP-(l), $NiCo_2S_{4-x}P_x$/CFP-(m) in 1 M KOH.

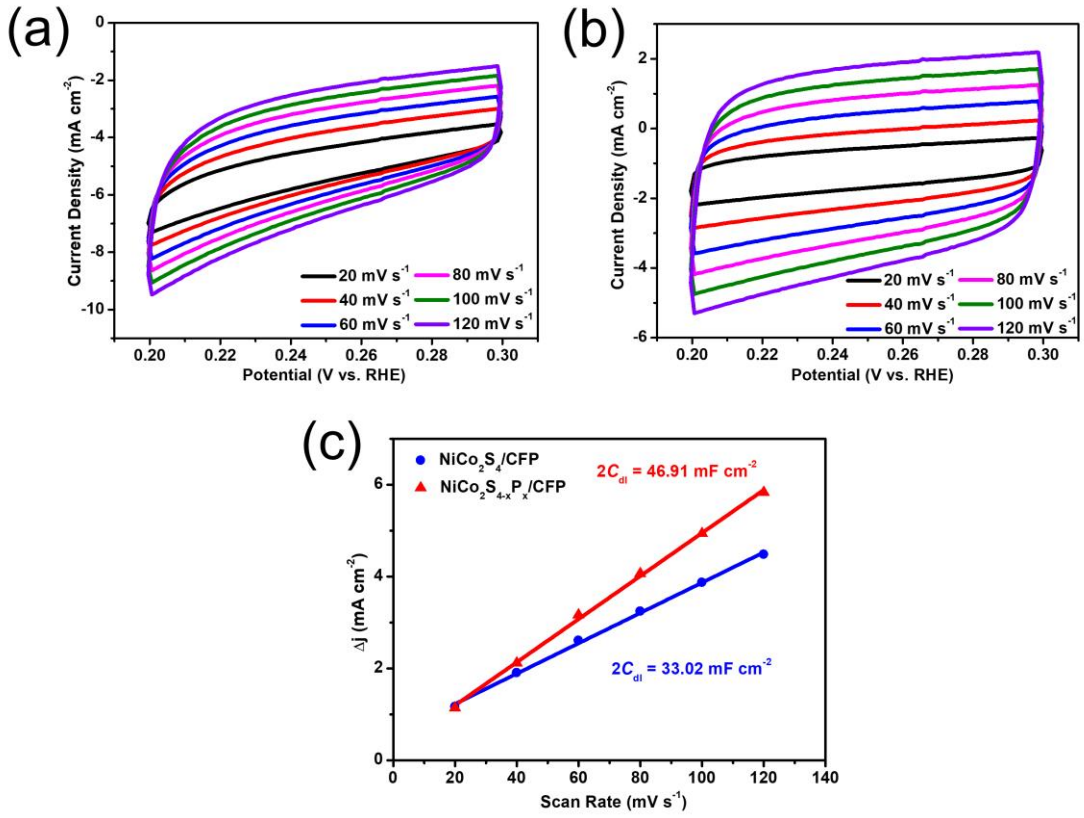

Figure S17. (a, b) CV curves of $NiCo_2S_4$/CFP (a) and $NiCo_2S_{4-x}P_x$/CFP (b) at different scan rates in 0.5 M H_2SO_4. (c) Calculated C_{dl} values of $NiCo_2S_4$/CFP and $NiCo_2S_{4-x}P_x$/CFP based on CV curves of (a, b) in 0.5 M H_2SO_4.

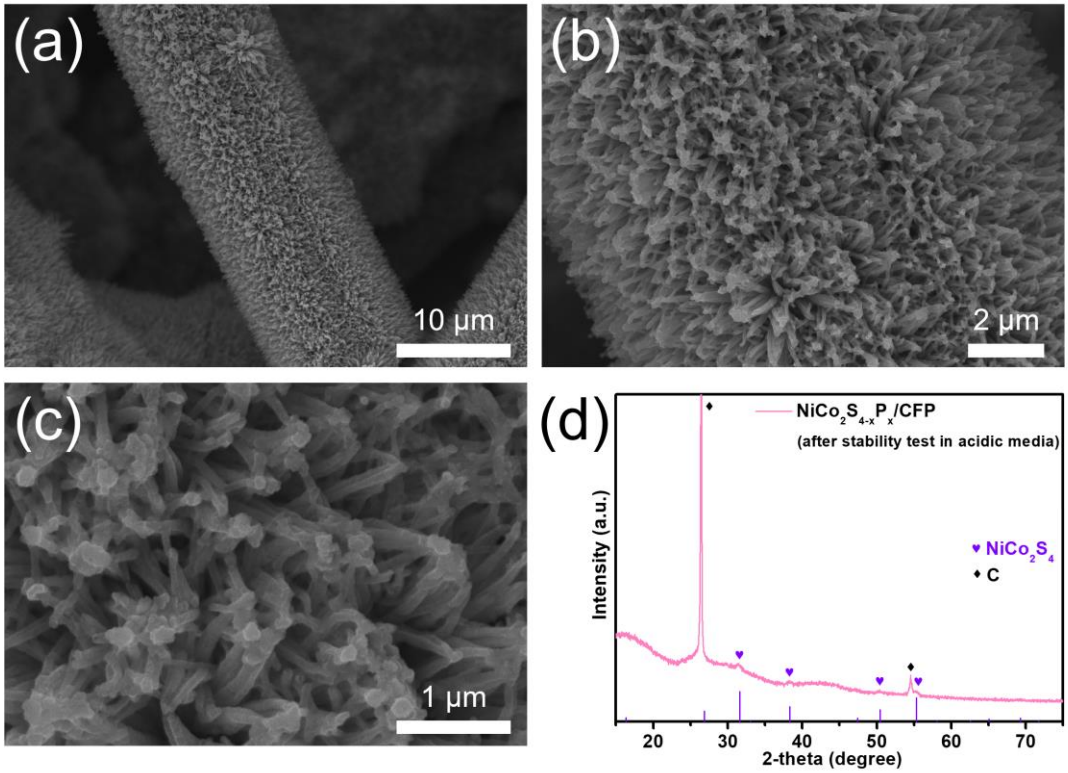

Figure S18. (a−c) SEM images of $NiCo_2S_{4-x}P_x$/CFP after HER stability test of 20 hours in 0.5 M H_2SO_4. (d) XRD pattern of $NiCo_2S_{4-x}P_x$/CFP after HER stability test of 20 hours in 0.5 M H_2SO_4.

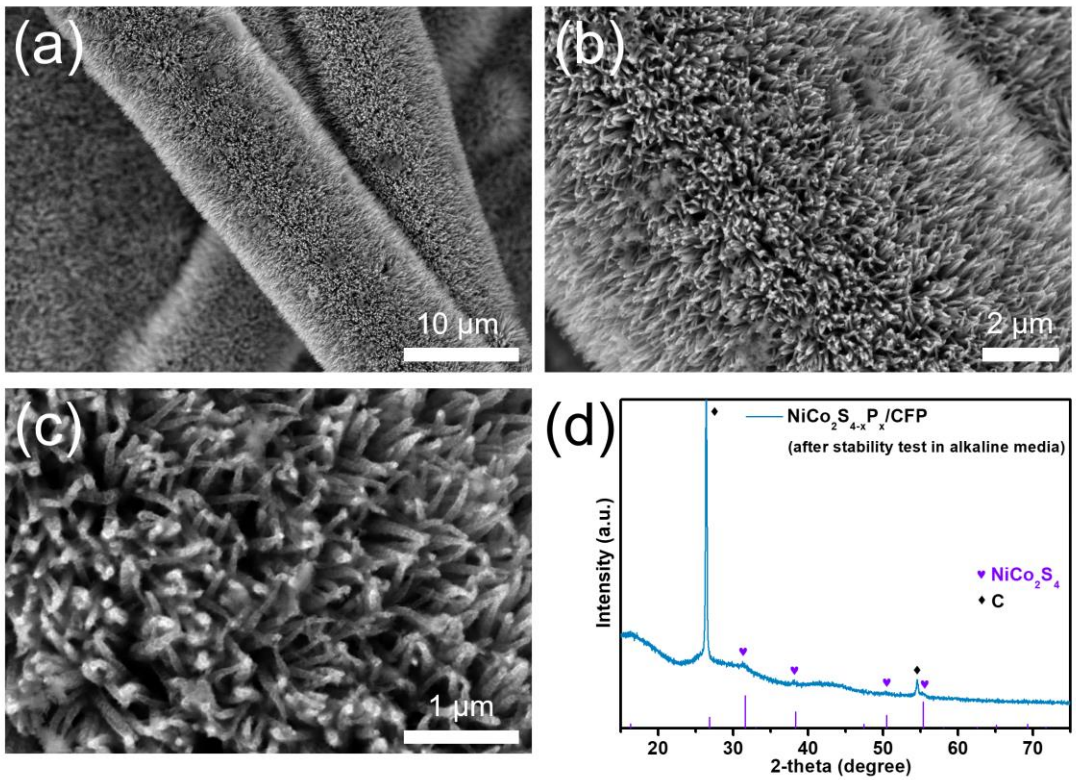

Figure S19. (a−c) SEM images of $NiCo_2S_{4-x}P_x$/CFP after HER stability test of 20 hours in 1 M KOH. (d) XRD pattern of $NiCo_2S_{4-x}P_x$/CFP after HER stability test of 20 hours in 1 M KOH.

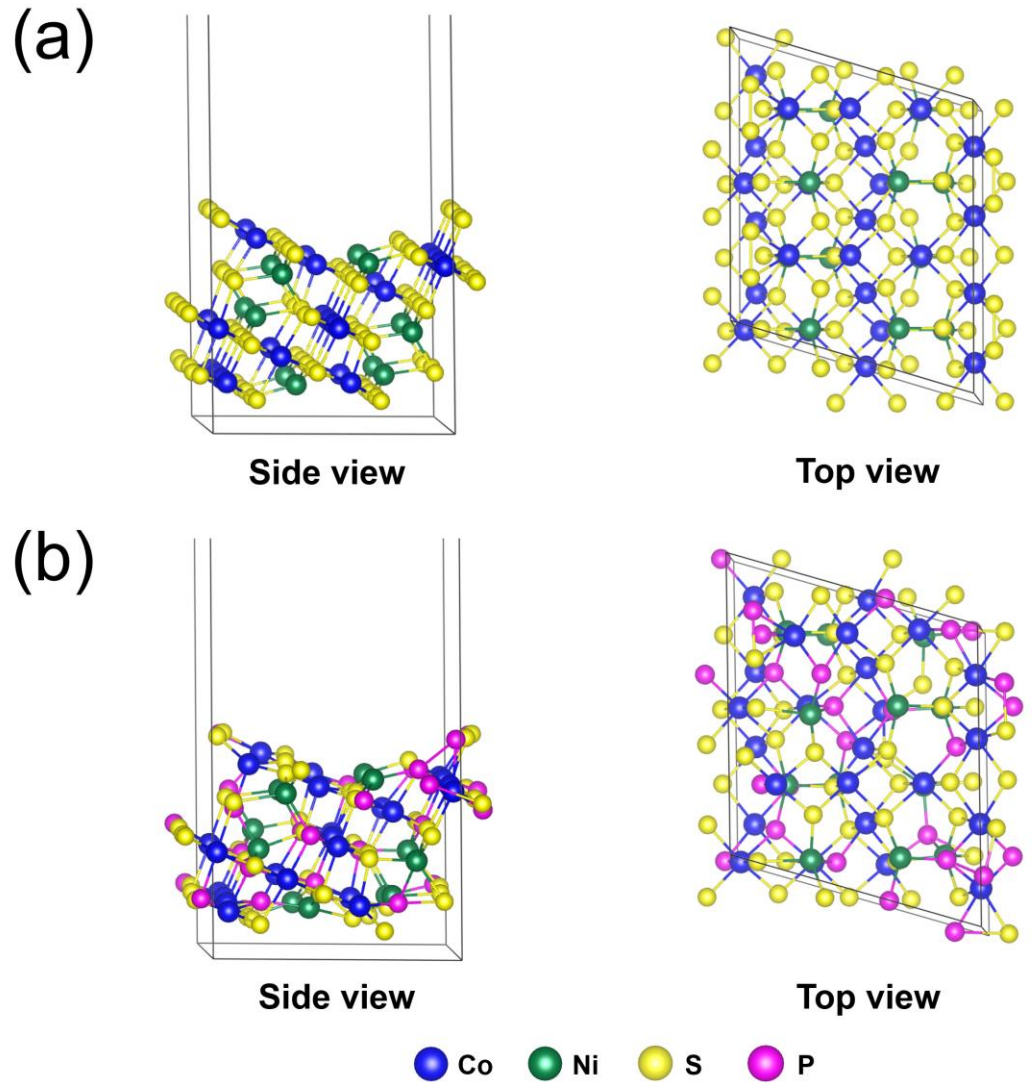

Figure S20. (a) Side view and top view of $NiCo_2S_4$ (311) surface. (b) Side view and top view of $NiCo_2S_{4-x}P_x$ (311) surface.

Table S1. XPS peak values of Co element from $NiCo_2S_{4-x}P_x$/CFP and $NiCo_2S_4$/CFP.

Catalyst	Peak	Binding Energy (eV)
$NiCo_2S_{4-x}P_x$/CFP	Co^{2+} $2p_{1/2}$	798.1
	Co^{2+} $2p_{3/2}$	781.8
	Co^{3+} $2p_{1/2}$	793.7
	Co^{3+} $2p_{1/2}$	778.6
	Satellite peaks	803.6
		785.6
$NiCo_2S_4$/CFP	Co^{2+} $2p_{1/2}$	798
	Co^{2+} $2p_{3/2}$	781.7
	Co^{3+} $2p_{1/2}$	793.9
	Co^{3+} $2p_{1/2}$	778.8
	Satellite peaks	803.6
		785.5

Table S2. XPS peak values of Ni element from $NiCo_2S_{4-x}P_x$/CFP and $NiCo_2S_4$/CFP.

Catalyst	Peak	Binding Energy (eV)
$NiCo_2S_{4-x}P_x$/CFP	Ni^{2+} $2p_{1/2}$	870.5
	Ni^{2+} $2p_{3/2}$	853.1
	Ni^{3+} $2p_{1/2}$	874.7
	Ni^{3+} $2p_{3/2}$	856.8
	Satellite peaks	880.9
		861.3
$NiCo_2S_4$/CFP	Ni^{2+} $2p_{1/2}$	870.6
	Ni^{2+} $2p_{3/2}$	853.3
	Ni^{3+} $2p_{1/2}$	875.2
	Ni^{3+} $2p_{3/2}$	857
	Satellite peaks	880.9
		861.5

Table S3. XPS peak values of S element from $NiCo_2S_{4-x}P_x$/CFP and $NiCo_2S_4$/CFP.

Catalyst	Peak	Binding Energy (eV)
$NiCo_2S_{4-x}P_x$/CFP	S^{2-} $2p_{1/2}$	162.5
	S^{2-} $2p_{3/2}$	161.4
$NiCo_2S_4$/CFP	S^{2-} $2p_{1/2}$	162.9
	S^{2-} $2p_{3/2}$	161.7
	S−O	169.8

Table S4. XPS peak values of P element from $NiCo_2S_{4-x}P_x$/CFP.

Catalyst	Peak	Binding Energy (eV)
$NiCo_2S_{4-x}P_x$/CFP	P $2p_{1/2}$	130.8
	P $2p_{3/2}$	129.7
	P−O	134.4

Table S5. HER overpotentials of catalysts in our work at different cathodic current densities (10, 100, 170 mA cm^{-2}) in 0.5 M H_2SO_4.

Catalyst	Overpotential (mV)		
	10 mA cm^{-2}	100 mA cm^{-2}	170 mA cm^{-2}
Pt	41	\	\
$NiCo_2S_4$/CFP	132	224	251
$NiCo_2S_{4-x}P_x$/CFP-(l)	88	172	212
$NiCo_2S_{4-x}P_x$/CFP-(m)	81	172	217
$NiCo_2S_{4-x}P_x$/CFP	80	168	202

Table S6. Comparison of the HER performances of $NiCo_2S_{4-x}P_x$/CFP with other reported sulfide-based electrocatalysts in 0.5 M H_2SO_4 aqueous solution.

Catalyst	Overpotential (mV) at 10 mA cm^{-2}	Tafel slope (mV dec^{-1})	Reference
$NiCo_2S_{4-x}P_x$/CFP	80	78.43	Our work
P-NCS/rGO	70	69	5
$(Ni_{0.33}Co_{0.67})S_2$ NWs/CC	81	60	6
P/CoS_2-5	109	48	7
Ni-S−P NRs/NF	107	47.6	8
Ni−Co_3S_4-15	224	81.2	9
CoS_x@MoS_2	239	103	10
Co_xS_y/WS_2/CC-3	120	89	11
NiS_2@MoS_2/CFP	95	65	12
Ni-MoS_2@CC-2	112	87	13
10% Mo-SnS	377	100	14

Table S7. HER overpotentials of catalysts in our work at different cathodic current densities (10, 100, 170 mA cm^{-2}) in 1 M KOH.

Catalyst	Overpotential (mV)		
	10 mA cm^{-2}	100 mA cm^{-2}	170 mA cm^{-2}
Pt	100	\	\
$NiCo_2S_4$/CFP	165	331	399
$NiCo_2S_{4-x}P_x$/CFP-(l)	138	238	281
$NiCo_2S_{4-x}P_x$/CFP-(m)	138	245	291
$NiCo_2S_{4-x}P_x$/CFP	132	228	267

Table S8. Comparison of the HER performances of $NiCo_2S_{4-x}P_x$/CFP with other reported sulfide-based electrocatalysts in 1 M KOH aqueous solution.

Catalyst	Overpotential (mV) at 10 mA cm^{-2}	Tafel slope (mV dec^{-1})	Reference
$NiCo_2S_{4-x}P_x$/CFP	132	84.36	Our work
$NiCo_2S_4$ NW/NF	210	58.9	3
$(Ni_{0.33}Co_{0.67})S_2$ NWs/CC	156	127	6
Ni−Co_3S_4-15	262	116.3	9
$NiCo_2S_4$@$NiCo_2S_4$/NF-2h	190	151.6	15
Fe, P-$NiCo_2S_4$	139	78.6	16
Fe doped-$NiCo_2S_4$	181	125	17
NiS/CoS/CC-3	102	114	18
$NiCo_2S_4$/Ni_3S_2/NF	119	105.2	19
P-Co_3S_4/CC	65	76.6	20
Ni:Co_3S_4	199	91	21

Table S9. The solution resistance (R_s) and charge transfer resistance (R_{ct}) values of $NiCo_2S_{4-x}P_x$/CFP and $NiCo_2S_4$/CFP in 0.5 M H_2SO_4 and 1 M KOH, respectively.

Electrolyte	Catalyst	R_s (Ω)	R_{ct} (Ω)
0.5 M H_2SO_4	$NiCo_2S_{4-x}P_x$/CFP	3.65	11.41
	$NiCo_2S_4$/CFP	3.97	100.00
1 M KOH	$NiCo_2S_{4-x}P_x$/CFP	3.61	29.36
	$NiCo_2S_4$/CFP	3.96	131.40

Note: The values in Table S9 are obtained from fitting equivalent circuit models in Figure 4g, h of the manuscript.

Table S10. Adsorption energies of hydrogen (ΔE_{H*}) and H_2O (ΔE_{H2O*}), Gibbs free energies of hydrogen adsorption (ΔG_{H*}) on different sites of $NiCo_2S_4$ (311) surface and $NiCo_2S_{4-x}P_x$ (311) surface, respectively, based on DFT calculations.

Surface	Site	ΔE_{H*} (eV)	ΔG_{H*} (eV)	ΔE_{H2O*} (eV)
$NiCo_2S_4$ (311)	Co	0.254	0.514	−0.419
	Ni	0.468	0.728	−0.315
	S	0.445	0.705	\
$NiCo_2S_{4-x}P_x$ (311)	Co	0.213	0.473	−0.438
	Ni	0.340	0.600	−0.389
	S	0.197	0.457	\
	P	−0.298	−0.038	\

References

1. K. Min, R. Yoo, S. Kim, H. Kim, S. E. Shim, D. Lim and S.-H. Baeck, *Electrochim. Acta*, 2021, **396**, 139236.
2. R. Chen, J. Xue, Y. Gong, C. Yu, Z. Hui, H. Xu, Y. Sun, X. Zhao, J. An, J. Zhou, Q. Chen, G. Sun and W. Huang, *J. Energy Chem.*, 2021, **53**, 226−233.
3. A. Sivanantham, P. Ganesan and S. Shanmugam, *Adv. Funct. Mater.*, 2016, **26**, 4661−4672..
4. L. Sha, K. Ye, G. Wang, J. Shao, K. Zhu, K. Cheng, J. Yan, G. Wang and D. Cao, *Chem. Eng. J.*, 2019, **359**, 1652−1658.
5. J. Chen, L. Mao, J. Xu, X. Gu, Z. I. Popov, Y. Zhao, Y. Ling, Y. Sui, P. Ying, X. Cai and J. Zhang, Sci. China Mater., 2023, 66, 3875−3886.
6. Q. Zhang, C. Ye, X. L. Li, Y. H. Deng, B. X. Tao, W. Xiao, L. J. Li, N. B. Li and H. Q. Luo, ACS Appl. Mater. Interfaces, 2018, 10, 27723−27733.
7. R. A. Senthil, J. Pan, Y. Wang, S. Osman, T. R. Kumar and Y. Sun, *Ionics*, 2020, **26**, 6265−6275.
8. Y. Zhou, T. Li, S. Xi, C. He, X. Yang and H. Wu, *ChemCatChem*, 2018, **10**, 5487−5495.
9. K. Ji, Q. Che, Y. Yue and P. Yang, *ACS Appl. Nano Mater.*, 2022, **5**, 9901−9909.
10. L. Yang, L. Zhang, G. Xu, X. Ma, W. Wang, H. Song and D. Jia, *ACS Sustainable Chem. Eng.*, 2018, **6**, 12961−12968.
11. X. Shang, J.-Q. Chi, S.-S. Lu, B. Dong, X. Li, Y.-R. Liu, K.-L. Yan, W.-K. Gao, Y.-M. Chai and C.-G. Liu, *Int. J. Hydrogen Energy*, 2017, **42**, 4165−4173.
12. H. Hu, J. Xu, Y. Zheng, Y. Zhu, J. Rong, T. Zhang, D. Yang and F. Qiu, *ACS Appl. Nano Mater.*, 2022, **5**, 10933−10940.
13. C. Yang, X. Tang, Z. Liu, R. Hao, J. Tian, C. Lin, M. Ma and W. Chen, *J. Electroanal. Chem.*, 2023, **932**, 117267.
14. S. R. Kadam, S. Ghosh, R. Bar-Ziv and M. Bar-Sadan, *Chem. Eur. J.*, 2020, **26**, 6679−6685.
15. X. Du, W. Lian and X. Zhang, *Int. J. Hydrogen Energy*, 2018, **43**, 20627−20635.

16. X. Feng, Y. Shi, J. Liang, W. Li and X. Gou, *J. Ind. Eng. Chem.*, 2023, **118**, 383−392.
17. L.-h. Qian, W.-w. Dong, H.-b. Li, X. Song and Y. Ding, *Int. J. Hydrogen Energy*, 2022, **47**, 8820−8828.
18. Y. Yang, H. Meng, Y. Zhang, Z. Li, Z. Zhang and Z. Hu, *Colloid Surface A*, 2020, **607**, 125452.
19. H. Liu, X. Ma, Y. Rao, Y. Liu, J. Liu, L. Wang and M. Wu, *ACS Appl. Mater. Interfaces*, 2018, **10**, 10890−10897.
20. Z. Guo, G. Tian, L. Liu, B. Zhang, Q. Wu, Y. Cao, J. Tu, L. Ding and X. Zhang, *J. Mater. Sci. Technol.*, 2021, **89**, 52−58.
21. S. Tang, X. Wang, Y. Zhang, M. Courté, H. J. Fan and D. Fichou, *Nanoscale*, 2019, **11**, 2202−2210.